

# Modeling the Transmission of Optical Lightning Signals through Complex Three-Dimensional Cloud Scenes

Michael Jay Peterson<sup>1</sup>

<sup>1</sup>LANL

November 22, 2022

## Abstract

Space-based lightning imagers have shown that complex cloud scenes that consist of multiple tall convective features, anvil clouds, and warm boundary cloud layers are illuminated by lightning in many different ways, depending on where the lightning occurs and how energetic it is. Modifications to the optical lightning signals from radiative transfer in the cloud medium can lead to reductions in detection efficiency and location accuracy for these instruments, and can also cause some of the optical signals that are detected to have unexpected spatial energy distributions. In this study, we perform Monte Carlo radiative transfer simulations of optical lightning emissions in clouds with complex three-dimensional geometries to shed some light on the origins of certain irregular radiance patterns that have been recorded from orbit. We show that reflections off nearby cloud faces can explain lightning signals in non-electrified clouds, tall clouds can result in poor optical transmission and suppressed radiances that could lead to missed events, and that particularly favorable viewing conditions can cause otherwise normal lightning to produce a “superbolt” that is orders of magnitude brighter than the same flash seen from a different direction.

1                   **Modeling the Transmission of Optical Lightning Signals through**  
2                   **Complex Three-Dimensional Cloud Scenes**

3  
4                   **Michael Peterson<sup>1</sup>**

5  
6                   <sup>1</sup>ISR-2, Los Alamos National Laboratory, Los Alamos, New Mexico  
7  
8  
9

10  
11  
12 Corresponding author: Michael Peterson (mpeterson@lanl.gov), B241, P.O. Box 1663 Los  
13 Alamos, NM, 87545  
14

15  
16 **Key Points:**

- 17                   • Lightning measurements from space have revealed complex interactions between optical  
18                   emissions and nearby clouds  
19                   • Monte Carlo radiative transfer simulations are conducted to examine how complex cloud  
20                   scenes are illuminated by lightning  
21                   • Modeling results support the suggested origins of irregular spatial radiance patterns and  
22                   unobscured lightning producing “superbolts”  
23  
24  
25

26 **Abstract**

27

28         Space-based lightning imagers have shown that complex cloud scenes that consist of  
29 multiple tall convective features, anvil clouds, and warm boundary cloud layers are illuminated  
30 by lightning in many different ways, depending on where the lightning occurs and how energetic  
31 it is. Modifications to the optical lightning signals from radiative transfer in the cloud medium  
32 can lead to reductions in detection efficiency and location accuracy for these instruments, and  
33 can also cause some of the optical signals that are detected to have unexpected spatial energy  
34 distributions. In this study, we perform Monte Carlo radiative transfer simulations of optical  
35 lightning emissions in clouds with complex three-dimensional geometries to shed some light on  
36 the origins of certain irregular radiance patterns that have been recorded from orbit. We show  
37 that reflections off nearby cloud faces can explain lightning signals in non-electrified clouds, tall  
38 clouds can result in poor optical transmission and suppressed radiances that could lead to missed  
39 events, and that particularly favorable viewing conditions can cause otherwise normal lightning  
40 to produce a “superbolt” that is orders of magnitude brighter than the same flash seen from a  
41 different direction.

42

43

44 **Plain Language Summary**

45

46 Lightning is detected from space using instruments that report rapid changes in cloud  
47 brightness from lightning illumination. However, this light can be modified by scattering and  
48 absorption in the cloud. Scattering off water drops causes portions of the signal to be diluted in  
49 space and delayed in time. What starts off as point impulsive light source in the cloud may  
50 illuminate a region of the cloud-top 100 km across with a waveform that lasts a significant  
51 fraction of a millisecond.

52 Interactions between the optical lightning emissions and the cloud scene are particularly  
53 complex when the surrounding clouds do not take on a simple geometric shape. Clouds observed  
54 in nature often contain multiple vertical layers including warm boundary clouds and overhanging  
55 anvils. Understanding some of the more irregular spatial energy distributions recorded by space-  
56 based lightning sensors requires accounting for these complex geometries.

57 In this study, we develop 3D cloud models that approximate cloud structures found in  
58 nature, and perform Monte Carlo radiative transfer simulations of how they are illuminated by  
59 lightning. In doing so, we confirm the suspected origins of irregular cloud illumination, such as  
60 reflections off of nearby cloud faces or particularly-favorable viewing conditions allowing  
61 normal lightning to appear highly-energetic.

62

## 63 **1 Introduction**

64

65 Pixelated lightning imagers including the Lightning Imaging Sensor (LIS: Christian et al.,  
66 2000; Blakeslee et al., 2014) and Geostationary Lightning Mapper (GLM: Goodman et al., 2013;  
67 Rudlosky et al., 2019) record the spatial distributions of optical energy that result from lightning  
68 pulses. These observed spatial radiance patterns often deviate from the simple idealized model of  
69 radiance decreasing only with radius from the center pixel. We previously reported cases of  
70 highly-irregular radiance patterns where the shape of the optical pulse on the CCD imaging array  
71 followed the cloud boundaries (i.e., Figures 3 and 4 in Peterson et al., 2017a), cases where the  
72 radiance pattern extended outward from the edge of the thunderstorm core giving an incorrect  
73 impression that these warm boundary clouds were producing lightning (Peterson et al., 2017b),  
74 and cases where optical emissions were blocked from reaching orbit by certain cloud regions,  
75 resulting in “holes” in otherwise-contiguous flash footprints (i.e., Figure 1 in Peterson and Liu,  
76 2013). Unobscured lightning sources have also been proposed as the mechanism responsible for  
77 certain lightning “superbolts” (Turman, 1977) that primarily illuminate the edge of the storm  
78 (Peterson et al., 2020).

79 Irregularities in lightning radiance patterns result from interactions between the optical  
80 lightning emissions and complex cloud scenes. Clouds modify optical lightning signals through  
81 absorption and scattering. While absorption prevents photons from reaching the space-based  
82 instrument entirely, multiple scattering diverts the photons from the direct path to the instrument.  
83 Some light will be redirected away from the sensor, while the signals that do arrive are  
84 broadened in space and diluted in time according to the path they took through the cloud. As  
85 clouds are invisible to Radio-Frequency (RF) signals, coordinated optical and RF measurements

86 have been used to quantify the severity of scattering delays (Suszcynsky et al., 2000; Light et al.,  
87 2001a) and to demonstrate reduced detection capabilities for optical space-based imagers when  
88 sources occur at low-altitudes in the cloud (Thomas et al., 2000).

89         Computational models have been employed to gain insights into how clouds modify  
90 optical lightning emissions. Thomson and Krider (1982) developed a Monte Carlo method for  
91 simulating optical transmission of transient light sources (both point sources and extended  
92 sources) through three-dimensional clouds of various geometries (cubic, spherical, and  
93 cylindrical). By measuring the path lengths taken by the emitted photons, they were able to  
94 further comment on typical scattering delays in the optical signals. Koshak et al. (1984)  
95 leveraged one-speed Boltzmann transport theory with diffusion approximations (essentially,  
96 treating the thundercloud as a nuclear reactor and replacing neutrons with photons) to model the  
97 waveforms that would be recorded from a high-altitude aircraft (or spacecraft) from spatially-  
98 complex lightning sources after scattering through homogeneous rectangular parallelepiped  
99 clouds. Light et al. (2001b) took a similar Monte Carlo approach to Thomson and Krider (1982),  
100 but, similar to Koshak et al. (1994), focused on the waveforms that would be measured by on-  
101 orbit sensors. Key to the present study, Light et al. (2001b) concluded that the shape of the cloud  
102 and position of the lightning event in the cloud (rather than the extent or motion of the source)  
103 are the primary factors that determine the distribution of photons escaping to space.

104         The primary limitation to these previous studies is that they represent homogeneous  
105 clouds with simple geometric shapes. Brunner and Bitzer (2020) used Weather Research and  
106 Forecasting (WRF) simulations of thunderstorms in a cubic model geometry to improve on how  
107 clouds were represented in Monte Carlo lightning illumination simulations by permitting  
108 inhomogeneous scattering media. However, they did not consider variations in cloud geometry,

109 and only reported the percentages of photons that escaped the upper cloud boundary – not how  
110 those photons were distributed across that boundary and would be imaged.

111         While a cylinder or even box geometry might approximate the structure of an isolated  
112 growing convective cloud, the cloud scenes monitored by LIS and GLM for lightning activity  
113 often consist of multiple convective cells with overhanging anvils that are also surrounded by  
114 warm boundary clouds. The simplistic clouds in these former model simulations are not  
115 sufficient to describe the complex interactions between the lightning emissions and the cloud  
116 scenes where we observe the irregular radiance patterns noted previously. The need for capturing  
117 complex cloud geometries was recognized by Light et al. (2001b) who stated “the  
118 most realistic [cloud] shape would be some superposition of cylindrical and planar.”

119         In this study, we ascertain which scenarios of lightning illuminating complex three-  
120 dimensional cloud scenes lead to the irregular radiance patterns that have been noted from orbit.  
121 We construct complex three-dimensional cloud shapes using composites of cylindrical and  
122 planar geometries to approximate cloud structures found in nature. These clouds are input into  
123 optical Monte Carlo radiative transfer simulations that yield spatial radiance measurements from  
124 a detector above the thunderstorm in physical units. By varying the optical thickness of the cloud  
125 layer and moving the lightning source around the three-dimensional scene, we are able to  
126 construct artificial radiance patterns that resemble the irregular features measured from orbit –  
127 including instances of reflections off neighboring clouds, poor transmission leading to holes in  
128 the image, and unobscured sources from normal lightning producing superbolts.

129

## 130 **2 Data and Methodology**

131           In this study, we use the Monte Carlo Atmospheric Radiative Transfer Simulator  
132 (MCARaTS: Iwabuchi, 2006; Iwabuchi and Okamura, 2017) to quantify the radiance that would  
133 be measured above the thunderstorm scene from an optical point source that approximates a  
134 lightning discharge. MCARaTS is a full three-dimensional radiative transfer simulator that uses a  
135 forward-propagating Monte Carlo photon transport algorithm to trace the trajectories of photon  
136 packets as they make their way across the scene until they are either absorbed or leave the  
137 atmosphere. The algorithm is capable of reproducing realistic 3-D effects including complex  
138 shadows and cloud side illumination (Iwabuchi, 2006). It is also adaptable for simulating a  
139 variety of optical and infrared sources including solar, thermal emission, and localized point  
140 sources.

141           MCARaTS inputs include models for the atmosphere and surface, and the simulation  
142 configuration that defines the properties of any light sources and imagers. In Section 2.1, we will  
143 detail the atmospheric models that we develop to represent complex cloud geometries. In Section  
144 2.2, we will describe the remaining general MCARaTS inputs. These inputs will also be  
145 summarized for quick reference in Table 1, below. Finally, in Section 2.3, we will describe the  
146 experimental configurations that will be used to examine variations in the optical radiance  
147 patterns produced by lightning.

### 148           2.1 Atmospheric Models with Complex Cloud Geometries

149           We consider five different cloud geometries that otherwise have identical vertical extents,  
150 compositions, and optical properties. To explore the dynamics of cloud geometry on measured  
151 lightning radiance, only the 3D extent of the cloud varies between cloud types. As with Light et

152 al., (2001b), we assume that each cloud consists of spherical water droplets evenly distributed  
153 throughout the cloud volume. Our cloud models will nominally be based on non-frontal water  
154 clouds whose drops have an effective radius of 10  $\mu\text{m}$ . The following sections describe the  
155 optical properties of these clouds as well as their 3D structure.

### 156 2.1.1 Scattering phase functions

157 Since we are concerned with cloud modifications to optical lightning signals, we assume  
158 that absorption and scattering takes place exclusively in the cloud layer. Photons in the free  
159 atmosphere will not be deflected from the forward direction or absorbed by atmospheric  
160 constituent gasses. Within the cloud layer, we assume that the phase functions for scattering  
161 interactions follow the Henyey-Greenstein approximation (van de Hulst, 1980) to the solution of  
162 the Mie scattering equations (Bohren and Huffman, 1983) below:

$$163 \quad p(\mu) = \frac{1 - g^2}{(1 + g^2 - 2g\mu)^{3/2}}$$

164 where  $\mu = \cos \alpha$ ,  $\alpha$  is the deflection angle relative to foreword transport, and  $g$  is the asymmetry  
165 parameter for the cloud particles in question at the specified wavelength of the simulation.

166 Thomson and Krider (1982) specified an asymmetry factor of 0.84 for 10  $\mu\text{m}$  water  
167 clouds illuminated by a near infrared (870 nm) source, while Light et al. (2001b) maintained this  
168 value for red photons. For consistency with past work, we will do the same. MCArTS requires  
169 phase functions to be specified as arrays of angle bins from 0° to 180°. For our simulations, we  
170 specify the Henyey-Greenstein solution with  $g = 0.84$  at an angular resolution of 1° per bin.

### 171 2.1.2 Atmospheric model

172 Atmospheric radiative transfer parameters are specified as 1D vertical profiles with  
173 perturbations listed on a 3D nested grid. Our models consist of 47 vertical layers that begin at the  
174 surface (0 km) and end at 30 km altitude. Within the lowest 10 km of the model domain, the  
175 layers are specified with a 250 m vertical resolution. Starting at 10 km, the layer spacing  
176 increases to 1 km. The final layers three are specified at a 10 km interval.

177 The 3D grid extends from the third vertical level (500 m) to the 24<sup>th</sup> vertical level (5750  
178 m). In each of these 3D layers, the horizontal grid is specified as a 60x60 element array. The  
179 horizontal resolution is defined in the model configuration. Nominally, we use a 200 m  
180 horizontal resolution, resulting in cloud scenes that are 12 km across. MCARaTS imposes a  
181 cyclic boundary condition for the 3D model (Iwabuchi, 2006), meaning that clouds and local  
182 sources within the model domain are infinitely tiled horizontally. This facilitates simulations of  
183 side illumination in neighboring clouds, for example from sources located at the cloud edge.

184 Since we are dealing with optical sources (rather than thermal sources), the three  
185 important parameters for our simulations are the phase function ( $p$ ) to be applied, the single  
186 scattering albedo ( $\bar{\omega}_o$ ), and the extinction coefficient ( $\sigma$ ). Each 1D layer and 3D gridpoint is  
187 assigned one of two states (within the cloud, or in the free atmosphere), and representative values  
188 for each of these parameters are prescribed based on this state. Inside the cloud, the Henyey-  
189 Greenstein phase function defined in the previous section is applied for  $p$ , and 0.99996 is  
190 selected for  $\bar{\omega}_o$ , again based on values from Thomson and Krider (1982) for 10  $\mu\text{m}$  water clouds  
191 illuminated by a near infrared source.

192 The extinction coefficient depends on the density and liquid water content of the clouds  
193 in question, and also determines the optical depth ( $\tau$ ) of the cloud. Light et al. (2001b)

194 constructed artificial drop size distributions by generating Gaussian functions centered on 10  $\mu\text{m}$ ,  
195 and then used these drop size distributions to calculate the photon mean free path between  
196 collisions with the spherical water drops. They noted that these drop size distributions are not  
197 realistic, but rather were selected to facilitate computations.

198         In this study, we instead take an observational approach to determine cloud extinction  
199 coefficients and optical depths. Plat (1997) parameterized aircraft observations of optical cloud  
200 characteristics according to effective drop size, water content, and atmospheric forcing. In their  
201 Figure 5, optical extinction coefficients are plotted for non-frontal water clouds based on  
202 measurements from Stephens et al. (1978). The observed extinction coefficients ranged from  $>$   
203  $0.01 \text{ m}^{-1}$  to  $< 0.08 \text{ m}^{-1}$ , while the parameterization for clouds with  $r_e = 10 \mu\text{m}$  drops bisects  
204 these aircraft data.

205         These values provide a reasonable range of extinction coefficients to consider in the  
206 present study. Light et al. (2001b) and Thomson and Krider (1982) noted that typical cloud  
207 optical depths vary from 80 to 400, and thus have been simulated in the literature. An optical  
208 depth of 80 (400) corresponds to a cloud extinction coefficient of  $0.015 \text{ m}^{-1}$  ( $0.076 \text{ m}^{-1}$ ) for a slab  
209 cloud in our 3D model geometry, thus filling the range of measured values from the aircraft data  
210 presented in Plat (1997). We simulate clouds with extinction coefficients throughout this range.  
211 The 1D  $\sigma$  profiles are specified as constant null values, while 3D  $\sigma$  perturbations are assigned  
212 constant values from this range (based on the experimental configuration) only in gridpoints  
213 within the cloud. Extinction coefficient perturbations in the 3D model domain outside of the  
214 cloud are assigned  $10^{-35} \text{ m}^{-1}$  (a minimum value corresponding to the numerical fill value in the  
215 simulation) due to constraints in the computational model.

## 216 2.1.3 Complex 3D Cloud Geometries

217 Five unique cloud types are constructed to account for finite / infinite geometries and the  
218 presence / absence of horizontal cloud layers at the top and bottom of the storm. The first cloud  
219 type is a simple infinite slab cloud. Such a cloud might stand in for stratiform clouds that are  
220 horizontally-expansive beyond the spatial scale of illumination from optical lightning pulses. The  
221 remaining four cloud types are represented as cylinders at the center of the 3D grid that fill all of  
222 its vertical layers. Images of these different cylinders are shown in Figure 1 using a wide-angle  
223 (180° FOV) camera located in the mid-levels of the 3D cloud model and pointed towards the  
224 horizon. The cylinders are illuminated from below the cloud base in Figure 1, while the camera  
225 response is normalized on a logarithmic scale to emphasize less-intense portions of the image.

226 The radius of these cylinders is set to 15 gridpoints (3000 m at the 200 m horizontal grid  
227 resolution). The default case (“Cylinder” in Figure 1a) lacks additional surfaces for scattering or  
228 reflections. In Figure 1b and d, a “base” cloud layer is added at the bottom of the cylinder. This  
229 base layer fills the bottom 4 vertical levels of the 3D model and has an infinite horizontal planar  
230 geometry. In Figure 1c and d, an “anvil” layer is added at the top of the cylinder. This anvil layer  
231 fills the top 5 vertical levels of the 3D model and has a cylindrical geometry with a radius of 22  
232 gridpoints (4400 m at the 200 m horizontal grid resolution).

## 233 2.2 Global MCARaTS inputs

234 The global inputs to MCARaTS – the source, surface, and imager – are specified below.  
235 While MCARaTS allows localized sources within the atmospheric model domain, it is not  
236 capable of simulating a fully-spherical isotropic source. To overcome this limitation, we model  
237 lightning emissions using two superimposed sources: one upward-facing point source, and one

238 downward-facing point source. We consider these light sources to be monochromatic near-  
239 infrared sources at 870 nm following Thomson and Krider (1982). These sources are assigned an  
240 optical power of  $10^9$  W, consistent with the order of magnitude in optical output from return  
241 strokes (i.e., Guo and Krider, 1982).

242 While surface reflections are not a focus of this study, we keep the stock seawater surface  
243 model that is included in the MCARaTS package. In Figure 1a, for example, a reflection off the  
244 surface can be noted below the cloud base. These surface reflections are only a second-order  
245 effect in our experiments. Except for the visualizations in Figure 1, all simulations place the  
246 imager at the top of the model domain (30 km) directly above the cloud center with nadir  
247 pointing. The imager records the radiance of each pixel across its Field of View (FOV). At the  
248 200 m horizontal grid spacing, a  $45^\circ$  full width FOV extends slightly beyond the edge of the  
249 horizontal model domain for the 3D cloud directly below the imager. For runs with a broader  
250 FOV or more compact clouds, we can image multiple clouds at different off-boresight angles.

### 251 2.3 Experimental configurations

252 Simulations are run to support three separate MCARaTS experiments. The model setup  
253 in these experiments is depicted in Figure 2. The source is shown as a double triangle symbol  
254 (representing the upward- and downward-directed sources), while the cylinder clouds directly  
255 below the imager are superimposed and outlined. The solid line shows the overall shape of the  
256 most-complex cloud type (Cylinder + Base & Anvil), and the dashed vertical lines show the  
257 edges of the primary cylinder cloud. These clouds shapes are repeated horizontally in all  
258 directions following the cyclic boundary conditions of the model.

259           There are two possible scenarios for the horizontal source location in each experiment. In  
260 Scenario A (Figure 2a), the source is placed at the geometric center of the cloud. In Scenario B  
261 (Figure 2b), the source is located near the edge of the inner cylinder. The position of the source  
262 in Scenario B is 1.8 grid points from the edge of the primary cylinder cloud (i.e., 360 m from the  
263 cylinder edge at the 200 m horizontal model resolution). The experiments / scenarios may be  
264 abbreviated by combining their designations (i.e., Experiment 2a or Experiment 3b).

265           The first experiment (Section 3.1) examines how the radiance patterns recorded by the  
266 imager above the cloud change for each cloud type according to the chosen cloud extinction  
267 coefficient and optical depth. In this experiment, we place the lightning source at the surface ( $z =$   
268 0 m) directly below the center of the cloud (Scenario A), and then record the radiance that is  
269 detected by the imager at 30 km altitude directly above the source. Experiment 1b is not  
270 performed.

271           The second experiment (Section 3.2) chooses an optical extinction coefficient from the  
272 first experiment to represent thick clouds, and then examines how the radiance patterns vary with  
273 (1) source altitude, and (2) source horizontal position. The source is free to move up and down  
274 the dotted vertical lines in Figure 2 between 0 km and 6 km altitude with a vertical step of 100  
275 m.

276           The third experiment (Section 3.3) leverages the tiled nature of the 3D model domain to  
277 examine how the radiance patterns vary with off-boresight angle relative to the nadir-pointing  
278 imager. The imager FOV is increased to a full width of  $120^\circ$  while the horizontal grid spacing of  
279 the 3D cloud model is reduced to 100 m between grid cells. This allows us to compare the

280 radiance from multiple clouds illuminated by identical lightning sources at various points across  
281 the instrument FOV when the source is located at either the center or the edge of the storm core.

282

### 283 **3 Results**

284 *3.1 Experiment 1: Radiance variations with cloud extinction coefficient and optical depth*

285           In the first experiment, we place our  $10^9$  W optical source below the cloud base at the  
286   geometric center of the storm and record the radiance patterns that result from simulations with  
287   different cloud extinction coefficients. This changes the optical depth of the cloud region that  
288   optical energy must transit to reach the imager. However, while it is expected that the central  
289   cylinder or slab will permit less energy from reaching orbit as the maximum optical depth of the  
290   scene increases, interactions with cloud edges and the base layer or anvil (if present) might  
291   enable photons to take shortcut paths to the imager. This would change how the flash appears  
292   from above, even though the brightness and position of the source and the geometric structure of  
293   the cloud remain unchanged.

294           Figure 3 shows how the recorded radiance from the imager pixel co-located with the  
295   source (solid lines) and the brightest pixel across the scene (dashed lines) vary with the  
296   prescribed cloud extinction coefficient for each of our cloud geometries. The received radiance  
297   from the center of the cloud decreases from  $\sim 1 \text{ Wm}^{-2}\text{sr}^{-1}$  at an optical depth of 80 to  $\sim 0.003 \text{ Wm}^{-2}\text{sr}^{-1}$   
298   at an optical depth of 400. Only slight differences can be noted between the cylindrical  
299   cloud types, while the slab geometry is slightly brighter than the other clouds at optical depths  
300   below  $\sim 250$ .

301           Because the model reports monochromatic radiance in physical units, we can put these  
302   values into perspective by comparing them with past observations of natural lightning. Christian  
303   and Goodman (1987) measured lightning from a high-altitude aircraft and reported peak  
304   radiances per flash over a range from  $< \sim 0.02 \text{ Wm}^{-2}\text{sr}^{-1}$  to  $0.3 \text{ Wm}^{-2}\text{sr}^{-1}$  and radiances from all  
305   pulses that extend down to  $< 0.005 \text{ Wm}^{-2}\text{sr}^{-1}$ . While key differences exist between these  
306   observations and our model in terms of source power (they estimated a median of  $10^8$  W, a factor

307 of 10 less than our model source), source altitude / extent, and cloud height, it is promising that  
308 the model radiances have a similar numerical range compared to these observations.

309         However, the center pixel directly over the source is only the brightest pixel in the scene  
310 when the cylindrical clouds have small optical depths. At optical depths around 200-250  
311 (depending on cloud geometry), the dashed curves in Figure 2 show the scene maximum  
312 radiance diverge from the solid curves that denote the source pixel radiance. By optical depths of  
313 400, the brightest pixels in the scene are an order of magnitude more radiant than the pixel  
314 directly over the source. Note that this does not occur with slab geometry clouds, where the  
315 source pixel remains the brightest point in the image at large optical depths.

316         To demonstrate why this is occurring, Figures 4 and 5 depict the radiance patterns  
317 produced by each cloud type for runs corresponding to an optical depth of 160 (Figure 4) and  
318 320 (Figure 5). The first five panels plot the radiance across the 3D model domain in imager  
319 pixel coordinates with the cloud type in question named in the plot title. Radiances are  
320 normalized according to the brightest pixel in each image. Dashed circles are drawn to show the  
321 diameters of the primary cylindrical cloud (at its base) and the cylindrical anvil cloud (where  
322 present). The geometric center of the cloud is indicated with asterisk symbols. The final sixth  
323 panel shows normalized radiance cross sections through the center of each image along the X  
324 axis. These cross sections are also indicated in the first five panels with horizontal dashed lines.

325         The clouds with the lower optical depths (Figure 4) are all brightest over the source and  
326 have radiance patterns that decrease radially with similar Gaussian curves out to near the edge of  
327 the primary cylindrical cloud (Figure 4f). The spatial radiance distributions diverge starting at  
328 this radius according to cloud geometry. While the cylindrical cloud (Figure 4b) drops

329 immediately to the model noise floor, clouds with a planar base (Figure 4c and e) have a  
330 secondary peak at the maximum cloud radius. If an overhanging anvil is present (Figure 4d and  
331 e), it can block radiance from reaching the imager, but illumination along its edges still  
332 contributes to the secondary radiance peak.

333         These radiance patterns change as we increase the cloud extinction coefficient and optical  
334 depth. The clouds in Figure 5 with maximum optical depths of 400 produce radiance peaks  
335 (Figure 5f) in the same locations as the previous cloud (Figure 4f), but the cloud edges are  
336 brighter than the central peak in all clouds with cylindrical geometries.

337         Here, we see the basis for holes in the lightning radiance patterns observed from space. If  
338 the radiance of these central pixels falls below the minimum sensitivity of the instrument, then it  
339 will only resolve the bright ring around the edge of the cloud. Figure 5c is particularly illustrative  
340 of what such a radiance pattern would look like in the lightning imager measurements. Pixels  
341 that correspond to shortcuts that the photons can take to avoid transmitting through the full  
342 optical depth of cloud will light up while the storm core remains dark. The implication of this is  
343 that poorly-transmissive clouds not only reduce the detection efficiency of the instrument, but  
344 also the location accuracy – as the pixels at the edge of the cloud are considered to have  
345 produced the optical impulse in question, when the source was actually located within the  
346 thunderstorm core.

347

### 348         3.2 Experiment 2: Radiance variations from source altitude

349         In the second experiment, we place our point source at various locations with each cloud  
350 geometry and then compare the radiance patterns recorded by the imager in each case. Figure 6a-

351 e compares the radiance from the pixel corresponding to the source location (solid lines) and the  
352 maximum scene radiance (dashed lines) in two scenarios for the horizontal source position: the  
353 source located at the geometric center of the cloud (Scenario A, black lines), and the source  
354 located near the edge of the primary cylindrical cloud (Scenario B, blue lines). Radiances are  
355 normalized relative to an unobscured source located at the cloud top. Figure 6f, then, computes  
356 the half width of half maximum (HWHM) in the resulting radiance pattern at each altitude and  
357 cloud type starting at 1500 m.

358         The radiance-altitude profiles show that the most rapid change in scene radiance occurs  
359 within the top 1 km of the cloud medium. When the source is located near the cloud top, the peak  
360 radiance is co-located with the source. Moreover, comparing the Experiment 2a curves (black)  
361 with the Experiment 2b curves (blue) suggests that this does not depend on the horizontal  
362 position of the source in the cloud. High-level sources behave as though they were embedded in  
363 slab clouds while their increased pixel radiances from having concentrated optical energies  
364 (Figure 6f) less diluted by the cloud medium provide a detection advantage over lower sources  
365 with the same optical power.

366         As the source is moved lower in the cloud, the curves for all finite cylindrical cloud  
367 geometries (Figure 6b-e) eventually separate. First, Scenario A begins to produce greater  
368 radiances than Scenario B, indicating additional energy loss from the instrument field of view  
369 when sources are placed near the edge of the scattering medium. Then, at a lower altitude, the  
370 source pixel loses its distinction as the brightest location in the scene. The altitudes where these  
371 separations occur, and the specific behavior of the Scenario B curves depend on the geometry of  
372 the cloud.

373         For Scenario A runs where the source is located at the geometric center of the cloud, the

374 scene maximum radiance curves separate from the source pixel radiance curves at ~2 km. Figure  
375 7 shows the radiance patterns from 2 km sources in each cloud type (Figure 7a-e) and a cross  
376 section through the center of the scene (Figure 7f) following the convention of Figures 4 and 5.  
377 While the central peak co-located with the source is still prominent, illumination of the cloud  
378 edges has become a significant feature in the spatial radiance distributions. By this altitude, the  
379 outer peak rivals the intensity of the central peak in clouds that have a base layer (Figure 7c and  
380 e). Moving the source further downward will eventually result in the radiance patterns from  
381 Figure 5 with the center peak almost completely eroded by the cloud optical depth.

382         The altitudes where the outer peak overtakes the central peak is particularly prevalent in  
383 the HWHM curves in Figure 6f. HWHM increases as sources are moved away from the cloud  
384 top. For sources above the cloud, this is due to reflections off the uppermost cloud boundary. For  
385 sources within the cloud, this is due to increased scattering interactions. Mid-level sources (i.e.,  
386 ~3 km altitude) have their radiant energy diluted over a large area through scattering, and this  
387 causes both a severe reduction in the maximum pixel radiance (only ~0.01% of an unobscured  
388 source) and large HWHM values (off-boresight angles of ~5° for our imager configuration and  
389 measurement geometry). However, when the outer peak becomes more radiant than the inner  
390 peak, the HWHM value suddenly increases because the HWHM algorithm is looking for the half  
391 maximum at radii beyond the peak radiance location. Ordered from highest to lowest altitude,  
392 this jump occurs first in Cylinder + Base clouds, then Cylinder + Base & Anvil clouds, then  
393 Cylinder clouds, and finally Cylinder + Anvil clouds. It does not occur with slab clouds. Thus,  
394 the presence of base cloud layers increases the altitude at which the cloud-edge peak overtakes  
395 the source pixel peak while anvils reduce this altitude.

396         While the Scenario B curves (blue lines) are less radiant than the Scenario A curves

397 (black) for sources near the tops of all cylindrical cloud geometries, radiances from low- to mid-  
398 level sources are greater in Scenario B. Reflections across the complex cloud scene are  
399 particularly important for these lower-altitude edge sources where reflective surfaces can allow  
400 the photons to take shortcuts to the imager.

401 Figure 8 demonstrates the role of reflections in the radiance patterns from offset lightning  
402 sources. In this case, the source is placed at 3.8 km altitude near the point where the blue curves  
403 separate in Figure 6b-e. Due to the cyclic nature of the 3D model domain, clouds and localized  
404 sources are repeated horizontally. Thus, the right side of the cloud is primarily illuminated by the  
405 visible source, while the left side of the cloud is primarily illuminated by the source in the next  
406 tile to the left (outside of the instrument FOV). For the slab cloud (Figure 8a), the radiance  
407 pattern is only influenced by the visible source. The radiance cross section (black line in Figure  
408 8f) decreases from the source location and remains near 0% at X pixels below 100.

409 While the finite cylindrical clouds have a radiance peak over the source, their radiance  
410 patterns and cross sections are irregular compared to the slab cloud case. For a simple cylindrical  
411 cloud (Figure 8b), the radiance peak over the source is bounded by the cloud edge, causing the  
412 cross section (Figure 8f) to be sharper on its right side. The radiance does not reach a minimum  
413 value immediately outside of the cloud because some radiance is reflected by the ocean surface,  
414 while a second prominent peak is visible along the left side of the cloud from radiance reflecting  
415 off the cloud face to reach the imager.

416 Adding a base cloud layer (Figure 8c) provides a more effective reflective surface for  
417 directing the lightning emissions towards the imager. The reflection off top of the base layer is  
418 more radiant than the primary peak co-located with the source (where the photons still must  
419 transit a relatively thick cloud layer to reach the imager). The neighboring point source still

420 illuminates the west edge of the cylindrical cloud, resulting in a total of three peaks in the X  
421 cross section in Figure 8f.

422         If we, instead, add an anvil to the top of the cylindrical cloud (Figure 8d), then the  
423 radiance peak over the source is not shifted as notably inward as in Figure 8b (though, the same  
424 effect applies at the edge of the wider anvil cloud). This case also results in three peaks in the  
425 radiance cross section in Figure 8f: the source peak, the right edge of the anvil cloud near the  
426 source, and the left edge of the anvil cloud reflecting radiance from the next source over. These  
427 latter two peaks are not as bright as the source peak.

428         Finally, if we add both a lower base layer and an upper anvil cloud to the simple cylinder  
429 cloud, the radiance pattern (Figure 8e) combines all of these effects. The source peak is nearly as  
430 radiant as in the anvil-only case (brighter than either the simple cylinder or base layer only  
431 geometries). However, while the anvil cloud blocks much of the radiance that reflects off of the  
432 lower base layer from reaching the imager, the second peak at the anvil cloud edge produces the  
433 strongest radiance in Figure 8f aside from the slab cloud source peak.

434         These radiance patterns show that increasing the complexity of the cloud scene provides  
435 more opportunities for the radiance pattern to diverge from the Gaussian spatial radiance  
436 distributions seen in slab clouds – especially when sources are offset from the geometric center  
437 of the cloud. The distinct variations between the radiance patterns from each cloud geometry  
438 discussed above further supports the idea that we can make inferences about cloud geometry and  
439 structure based on how the clouds are illuminated by lightning.

440

### 441         3.3 Experiment 3: Radiance variations from look angle

442         The first two experiments consider how clouds directly below the imager are illuminated

443 by lightning sources. In the third experiment, we expand the imager FOV while decreasing the  
444 horizontal grid spacing of the cloud model to image multiple clouds illuminated by surface-level  
445 sources at various points across the scene.

446 Radiance patterns from Scenario A (centered lightning source) are shown in Figure 9 for  
447 each of our cloud geometries. Because the imager has a square shape with each axis (X and Y)  
448 covering  $120^\circ$ , the corner pixels (outside of the inner dashed circle) extend out beyond this  
449 nominal angular FOV. The horizon below the camera ( $\sim 75^\circ$  from nadir) can be noted in the  
450 corners of the image (outer dashed line) where the illuminated clouds seem to disappear from the  
451 image. Each of the images in Figure 9a-e are normalized relative to the brightest pixel in the  
452 image, as before. However, instead of a cross section through the center of the image, the final  
453 panel (Figure 9f) shows the peak radiance in each ring corresponding to a particular off-boresight  
454 angle.

455 A common feature for all finite cylindrical cloud types (Figure 9b-e) is that the center  
456 cloud that we examined in Experiments 1 and 2 is the least radiant cloud in the scene. Clouds  
457 that are not located at nadir provide more shortcut paths that photons can take to the imager. As a  
458 result, less of the radiance is diluted or extinguished from the instrument FOV. The radial  
459 distribution of peak radiance (Figure 9f) is similar for all cloud types for the first three peaks (up  
460 to  $\sim 45^\circ$ ). Within this range, the peak radiance from all cloud tiles (except the cloud at nadir) is  
461 approximately the same and does not notably increase with the off-boresight angle of the cloud  
462 in question.

463 However, not all cloud tiles in the image achieve these peak radiance values. Particularly  
464 along the central X and Y axes in Figure 9b-e (pixel coordinate 400), the clouds near the edge of  
465 the nominal X and Y FOV ( $60^\circ$ ) have their radiance blocked by the top of the neighboring cloud

466 closer to the center of the image. This blocking is especially important for cloud types with anvil  
467 layers (Figure 9d and e) because the cylindrical anvils at the cloud top have an increased  
468 diameter compared to the primary cylindrical cloud.

469         These competing factors – the relative visibility of the source and blocking by  
470 neighboring clouds – cause the angular peak radiance distributions for each cloud type to diverge  
471 at off-boresight angles beyond  $45^\circ$ . The key factor for how the radiance distributions behave  
472 after this point is whether the cloud geometry has a base layer. If no base layer is present, then  
473 the peak radiance begins to increase with off-boresight angle, as the source is less obscured when  
474 the cloud is viewed from the side. Anvil clouds (if present) are more effective at blocking  
475 radiance at large off-boresight angles than narrow cylinders. Thus, the Cylinder cloud type (blue  
476 line in Figure 9f) reaches a maximum peak radiance between the nominal ( $60^\circ$ ) and overall ( $75^\circ$ )  
477 edge of the imager FOV that is 4x brighter than any other cloud type, while the Cylinder + Anvil  
478 cloud type (red line) angular peak radiance distribution decreases.

479         If a base layer is present, however, then the angular peak radiance distributions do not  
480 notably increase beyond off-boresight angles of  $45^\circ$ . The various peaks in these distributions  
481 (corresponding to unique cloud tiles) maintain their off-nadir values from angles  $< 45^\circ$ . It should  
482 be noted that these trends are only valid for the cloud tile spacing and measurement geometry  
483 considered by these simulations. Radiance certainly changes significantly with off-boresight  
484 angle when the imager is located at higher altitudes.

485         Figure 10 depicts the radiance patterns that result from Scenario B where the source is  
486 placed near the (right) edge of the primary cylindrical cloud. Blocking by neighboring clouds is  
487 particularly important when the source is located at the edge of the storm. Tiles where entire  
488 cloud volumes separate the source from the imager remain dark – including most of the right side

489 of the imager FOV and also sources along the central X axis at pixel coordinates < 200.  
490 However, this blocking is not evident in Figure 10b and d because it is overshadowed by  
491 extremely-bright pixels in the tiles to the left of center. These pixels have a direct sight line on  
492 the lightning source. When the base layer is present, it dilutes the optical emissions from the  
493 offset source, causing the peak radiance profiles for the Cylinder + Base and Cylinder + Base &  
494 Anvil cloud geometries in Figure 10f to behave in a similar manner to the slab cloud geometry  
495 (black curve) – only at a greater radiance due to its thin vertical extent. Without this base layer,  
496 the Cylinder and Cylinder + Anvil cloud geometries record the unimpeded radiance from the  
497 source. Indeed, the maximum values in their angular peak radiance distributions (blue and red  
498 curves) nearly reach 100% of the radiance of the unobstructed cloud-top source.

499         We are, essentially, describing the conditions that allow ordinary lightning to be  
500 measured as a “superbolt.” Having this direct unobscured line on the source can cause the peak  
501 radiance to be 5 orders of magnitude brighter than the same exact source below a cloud layer –  
502 either on the edge of the storm but below a base layer of warm cloud, or centered in the storm  
503 core (Figure 9). Since superbolts are defined as being 2-3 orders of magnitude brighter than  
504 typical lightning, this scenario may allow normal lightning to contribute significantly to the  
505 sample of superbolts recorded from space by optical instruments. This is not the only scenario  
506 where a superbolt can arise (particularly powerful lightning sources embedded in the cloud layer  
507 can achieve similarly-bright radiances) but it confirms our explanation of “anvil superbolts” that  
508 are exceptionally bright while primarily illuminating cloud regions at the edge of the  
509 thunderstorm (Peterson et al., 2020).

510

## 511 4 Conclusion

512 This study uses optical Monte Carlo radiative transfer simulations with complex three-  
513 dimensional cloud scenes to explain the origins of irregular lightning radiance patterns that have  
514 been observed from orbit – including “holes” in the middle of otherwise-contiguous illuminated  
515 cloud regions, lightning that wraps around storm edges or seems to occur entirely in a warm  
516 boundary cloud that is probably not electrified, and particularly-intense lightning signals from  
517 storm edges (“anvil superbolts”). We approximate the shapes of natural stormclouds by  
518 combining cylindrical and slab cloud geometries. While a purely-cylindrical cloud might  
519 approximate growing convection, tall convection with an overhanging anvil is simulated by  
520 adding a second cylinder with a greater diameter at the top layers of the cloud. Warm boundary  
521 clouds, then, are simulated by adding an infinite slab cloud to the bottom of the primary cylinder.

522 These clouds are illuminated by localized point sources that approximate lightning  
523 emissions, and the radiance patterns measured by an imager above the cloud are recorded. By  
524 varying the optical thickness of the clouds and moving the point source around the cloud scene,  
525 we are able to explore the dynamics of cloud illumination and identify scenarios that result in the  
526 irregular radiance patterns of interest.

527 We confirm that reflections off of nearby cloud faces (particularly the lower warm  
528 boundary cloud) are an important factor that determines how the radiance measured from above  
529 is distributed spatially across the scene. When the source is located below a thick storm cloud,  
530 the brightest illumination in the scene is from “shortcuts” that the optical signals can take to  
531 reach the imager without scattering through the entire cloud depth. This is important because  
532 mid-level sources reflecting off a base layer or low-level CG sources might appear to be located  
533 outside of the storm core when the primary peak directly over the source is attenuated, reducing

534 location accuracy. Moreover, particularly thick clouds almost entirely attenuate this peak,  
535 resulting in the “hole” features noted in observations. Even though overhanging anvils are a  
536 “shortcut” due to their limited optical depth compared to the full cylinder, they still extinguish  
537 the signals from low-level sources and can form holes by reflecting radiance back towards the  
538 Earth.

539         On the other extreme, certain viewing geometries can lead to particularly favorable  
540 shortcut paths where the imager can view a source located at the edge of the storm directly  
541 without significant modification by the clouds. Because the measured radiance decreases  
542 exponentially in the first ~1 km of cloud between the source and sensor, the radiance from such  
543 an unobstructed source is up to 5 orders of magnitude brighter than the same source viewed from  
544 a different angle. Thus, a normal lightning source that is observed along this particularly  
545 favorable sight line can easily be labeled as a superbolt – and this appears to be the origin of our  
546 “anvil superbolts” that primarily illuminate the edges of the parent thunderstorm.

547         These results show that increasing the complexity of the cloud scene provides more  
548 opportunities for complex interactions with the lightning emissions, and thus increased  
549 complexity in the resulting radiance pattern measured from above the storm. However, when the  
550 clouds can be represented as slab layers (for example, stratiform clouds or high-altitude sources),  
551 radiance profiles can be approximated with Gaussian curves. These findings support the idea that  
552 we can infer cloud structure based on how the clouds are illuminated by lightning (i.e., how the  
553 radiance pattern diverges from an idealized state).

554

555 **Acknowledgments**

556 This work was supported by the US Department of Energy through the Los Alamos National  
 557 Laboratory (LANL) Laboratory Directed Research and Development (LDRD) program under  
 558 project number 20200529ECR. Los Alamos National Laboratory is operated by Triad National  
 559 Security, LLC, for the National Nuclear Security Administration of U.S. Department of Energy  
 560 (Contract No. 89233218CNA000001). The MCArTS model used in this study may be acquired  
 561 from its website (<https://sites.google.com/site/mcarats/home>), while the cloud models that serve  
 562 as input data are located at Peterson (2020).

563 **References**

- 564 Brunner K., & P. M. Bitzer (2020). A first look at cloud inhomogeneity and its effect on  
 565 lightning optical emission. *Geophysical Research Letters*, 47, e2020GL087094.  
 566 <https://doi.org/10.1029/2020GL087094>
- 567 Bohren, C. F., and D. R. Huffman (1983): Absorption and scattering by a sphere. In *Absorption*  
 568 *and Scattering of Light by Small Particles*, pp.82-129, John Wiley, New York.
- 569 Christian, H.J. and S.J. Goodman, 1987: [Optical Observations of Lightning from a High-Altitude](https://doi.org/10.1175/1520-0426(1987)004<0701:OOOLFA>2.0.CO;2)  
 570 [Airplane](https://doi.org/10.1175/1520-0426(1987)004<0701:OOOLFA>2.0.CO;2). *J. Atmos. Oceanic Technol.*, 4, 701–711, [https://doi.org/10.1175/1520-](https://doi.org/10.1175/1520-0426(1987)004<0701:OOOLFA>2.0.CO;2)  
 571 [0426\(1987\)004<0701:OOOLFA>2.0.CO;2](https://doi.org/10.1175/1520-0426(1987)004<0701:OOOLFA>2.0.CO;2)
- 572 Christian, H. J., R. J. Blakeslee, S. J. Goodman, and D. M. Mach (Eds.), 2000: Algorithm  
 573 Theoretical Basis Document (ATBD) for the Lightning Imaging Sensor (LIS),  
 574 NASA/Marshall Space Flight Center, Alabama. (Available as  
 575 <http://eosps0.gsfc.nasa.gov/atbd/listables.html>, posted 1 Feb. 2000)
- 576 Goodman, S. J., R. J. Blakeslee, W. J. Koshak, D. Mach, J. Bailey, D. Buechler, L. Carey, C.  
 577 Schultz, M. Bateman, E. McCaul Jr., and G. Stano, 2013: The GOES-R geostationary  
 578 lightning mapper (GLM). *J. Atmos. Res.*, **125-126**, 34-49
- 579 Guo, C., and Krider, E. P. (1982), The optical and radiation field signatures produced by  
 580 lightning return strokes, *J. Geophys. Res.*, 87(C11), 8913– 8922,  
 581 doi:[10.1029/JC087iC11p08913](https://doi.org/10.1029/JC087iC11p08913).
- 582 Iwabuchi, H., 2006: Efficient Monte Carlo methods for radiative transfer modeling. *J. Atmos.*  
 583 *Sci.*, **63**, 2324-2339.
- 584 Iwabuchi, H., and R. Okamura, 2017: Multispectral Monte Carlo radiative transfer simulation by  
 585 using the maximum cross-section method. *Journal of Quantitative Spectroscopy and*  
 586 *Radiative Transfer*, 193, 40–46, . doi: 10.1016/j.jqsrt.2017.01.025
- 587 Light, T. E., Suszcynsky, D. M., and Jacobson, A. R. (2001a), Coincident radio frequency and  
 588 optical emissions from lightning, observed with the FORTE satellite, *J. Geophys. Res.*,  
 589 106(D22), 28223– 28231, doi:[10.1029/2001JD000727](https://doi.org/10.1029/2001JD000727).
- 590 Light, T. E., Suszcynsky, D. M., Kirkland, M. W., and Jacobson, A. R. (2001b), Simulations of

591 lightning optical waveforms as seen through clouds by satellites, *J. Geophys. Res.*, 106(  
 592 D15), 17103– 17114, doi:[10.1029/2001JD900051](https://doi.org/10.1029/2001JD900051).

593 Peterson, M., (2020): Cloud Models used in Lightning Radiative Transfer Simulations.  
 594 <https://doi.org/10.7910/DVN/0RU44I>, Harvard Dataverse, DRAFT VERSION

595 Peterson, M., and Liu, C. ( 2013), Characteristics of lightning flashes with exceptional  
 596 illuminated areas, durations, and optical powers and surrounding storm properties in the  
 597 tropics and inner subtropics, *J. Geophys. Res. Atmos.*, 118, 11,727– 11,740,  
 598 doi:[10.1002/jgrd.50715](https://doi.org/10.1002/jgrd.50715).

599 Peterson, M., Rudlosky, S., & Deierling, W. ( 2017a). The evolution and structure of extreme  
 600 optical lightning flashes. *Journal of Geophysical Research: Atmospheres*, 122, 13,370–  
 601 13,386. <https://doi.org/10.1002/2017JD026855>

602 Peterson, M., Rudlosky, S., & Zhang, D. ( 2020). Changes to the appearance of optical lightning  
 603 flashes observed from space according to thunderstorm organization and structure.  
 604 *Journal of Geophysical Research: Atmospheres*, 125, e2019JD031087.  
 605 <https://doi.org/10.1029/2019JD031087>

606 Platt, C.M., 1997: [A Parameterization of the Visible Extinction Coefficient of Ice Clouds in  
 607 Terms of the Ice/Water Content](https://doi.org/10.1175/1520-0469(1997)054<2083:APOTVE>2.0.CO;2). *J. Atmos. Sci.*, **54**, 2083–2098,  
 608 [https://doi.org/10.1175/1520-0469\(1997\)054<2083:APOTVE>2.0.CO;2](https://doi.org/10.1175/1520-0469(1997)054<2083:APOTVE>2.0.CO;2)

609 Rudlosky, S. D., S. J. Goodman, K. S. Virts, and E. C. Bruning, 2018: Initial geostationary  
 610 lightning mapper observations. *Geophys. Res. Lett.*, **46**, 1097– 1104.  
 611 <https://doi.org/10.1029/2018GL081052>

612 Stephens, G. L., G. W. Paltridge, and C. M. R. Platt, 1978: Radiation profiles in extended water  
 613 clouds, III. Observations. *J. Atmos. Sci.*, **35**,2133–2141.

614 Suszycynsky, D. M., Kirkland, M. W., Jacobson, A. R., Franz, R. C., Knox, S. O., Guillen, J. L.  
 615 L., and Green, J. L. ( 2000), FORTE observations of simultaneous VHF and optical  
 616 emissions from lightning: Basic phenomenology, *J. Geophys. Res.*, 105( D2), 2191–  
 617 2201, doi:[10.1029/1999JD900993](https://doi.org/10.1029/1999JD900993).

618 Thomas, R., P.R. Krehbiel, W. Rison, T. Hamlin, D. J. Boccippio, S. J. Goodman, and H. J.  
 619 Christian, 2000: Comparison of ground-based 3-dimensional lightning mapping  
 620 observations with satellite-based LIS observations in Oklahoma. *Geophys. Res. Lett.*, **27**,  
 621 12, 1,703-1,706.

622 Thomson, L.W. and E.P. Krider, 1982: [The Effects of Clouds on the Light Produced by  
 623 Lightning](https://doi.org/10.1175/1520-0469(1982)039<2051:TEOCOT>2.0.CO;2). *J. Atmos. Sci.*, **39**, 2051–2065, [https://doi.org/10.1175/1520-  
 624 0469\(1982\)039<2051:TEOCOT>2.0.CO;2](https://doi.org/10.1175/1520-0469(1982)039<2051:TEOCOT>2.0.CO;2)

625 Turman, B. N. ( 1977), Detection of lightning superbolts, *J. Geophys. Res.*, 82( 18), 2566– 2568,  
 626 doi:[10.1029/JC082i018p02566](https://doi.org/10.1029/JC082i018p02566).

627 van de Hulst, H. C. (1980). Multiple Light Scattering, vols. 1 and 2, Academic, San Diego, Calif.  
 628  
 629  
 630  
 631  
 632  
 633  
 634  
 635  
 636

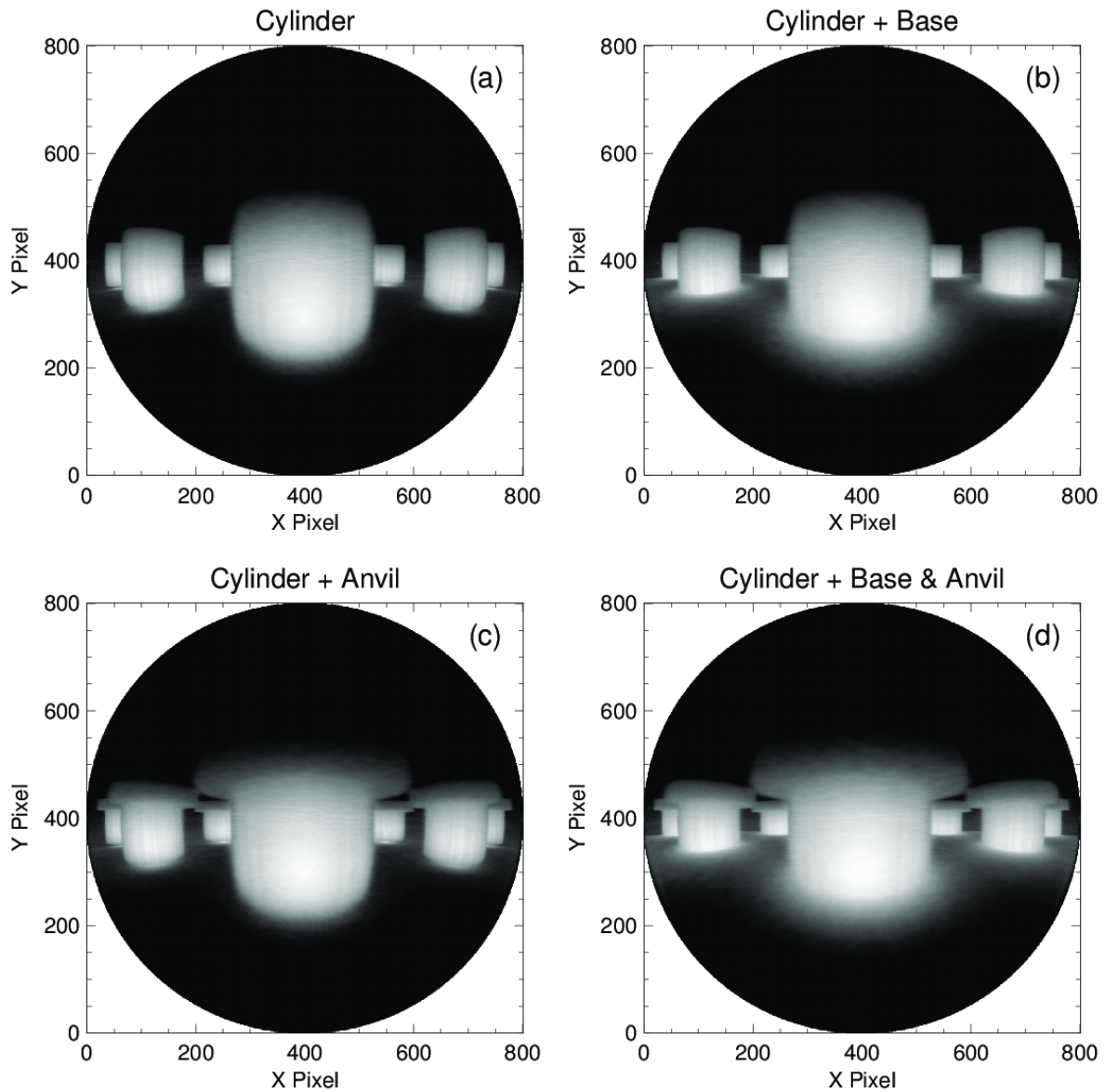
637  
638  
639  
640

641 **Table 1.** Inputs into the MCARaTS model that define the point source, atmospheric model, and  
 642 optical imager.  
 643

Configuration Parameter	Nominal Value		Resolution / Delta	
	Clear Air	Cloud	Clear Air	Cloud
<b>POINT SOURCE:</b>				
Power	1e9 W		-----	
Wavelength	6670 nm		Monochromatic	
<b>ATMOSPHERIC MODEL:</b>				
1-D Vertical Layers	47 layers from 0 – 30 km		250 m [0-10 km], 1 km [10-15 km], 10 km [10-30 km]	
3-D Vertical Layers	21 layers starting at 500 m altitude		250 m	
3-D Horizontal Grid	60 x 60 square grid with infinite horizontal repetition		100-200 m	
Phase Function	Foreword transport only	Henye- Greenstein Mie scattering approximation	1° per angle bin	
Asymmetry Factor (g)	-----	0.84	-----	-----
Single-Scattering Albedo ( $\bar{\omega}_o$ )	-----	0.99996	-----	-----
Extinction Coefficient	1.e-35 m <sup>-1</sup> (numerical fill value)	Variable, 0.01 – 0.08 m <sup>-1</sup>	-----	-----
Maximum Vertical Extent	-----	5,250 m	-----	-----
Maximum Optical Depth	-----	52 – 420	-----	-----
<b>IMAGER:</b>				
Field of View Full Width	45°, 120°		0.14° per pixel	
Altitude	30 km		-----	
Pointing	Nadir		-----	

644  
 645  
 646  
 647

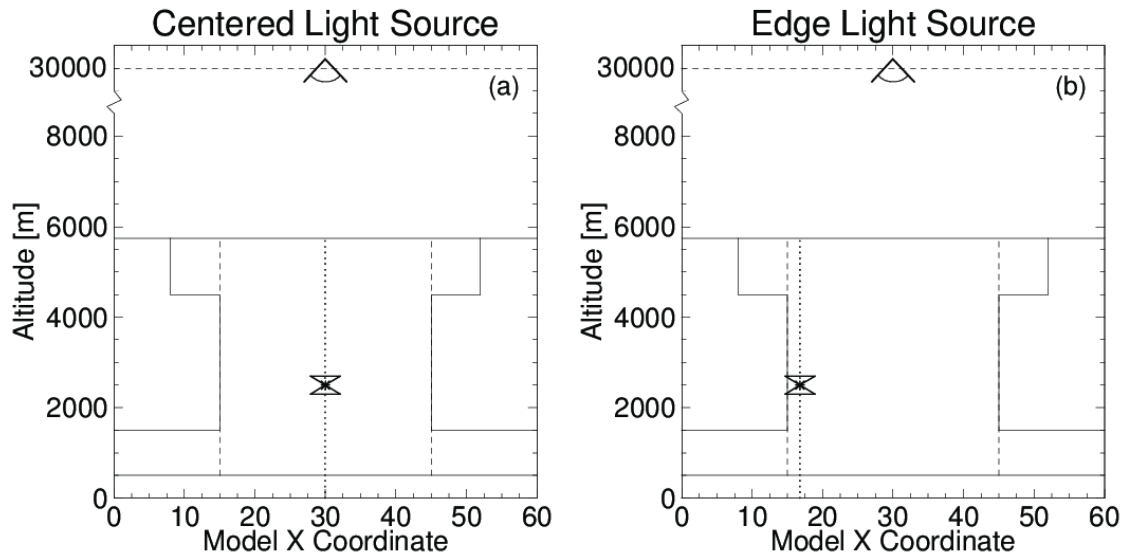
648



649  
650  
651  
652  
653  
654

**Figure 1.** Visualization of the geometries of the finite cylindrical clouds. A wide angle ( $180^\circ$ ) camera is placed at the mid-level of the 3D cloud domain and pointed towards the horizon. The radiance from the Cylinder (a), Cylinder + Base (b), Cylinder + Anvil (c) and Cylinder + Base & Anvil illuminated from below are recorded with a logarithmic normalization.

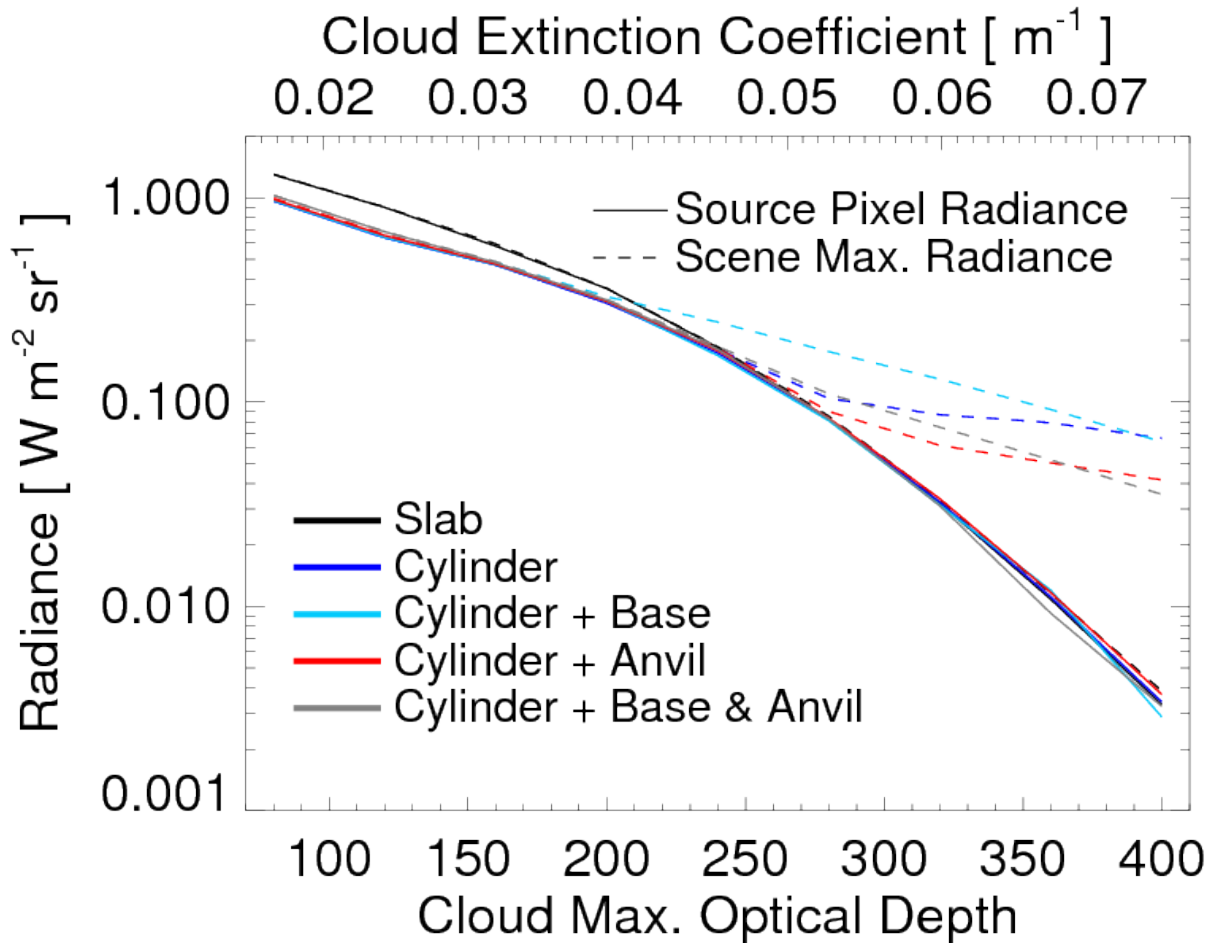
655



656  
 657  
 658  
 659  
 660  
 661  
 662  
 663

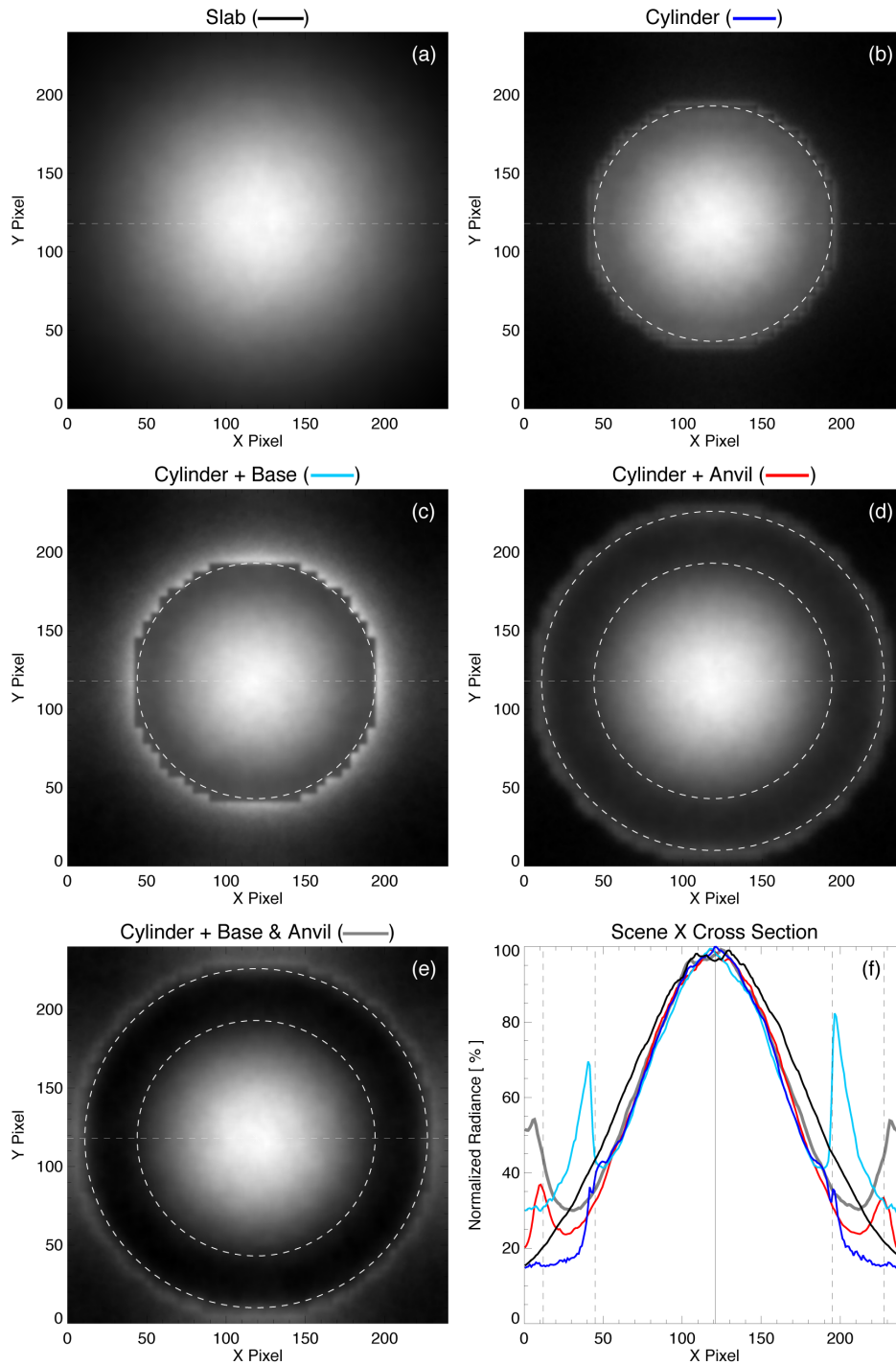
**Figure 2.** Experimental setup showing the location of the light source (double triangle) and imager (eye symbol) in the cylindrical cloud geometries for (a) Scenario A where the source is at the geometric center of the cloud, and (b) Scenario B where the source is located near the edge of the primary cylinder. Solid lines outline the outer boundaries of the slab and most complex cylindrical clouds while dashed lines show the primary cylinder radius. Dotted lines indicate the range of altitudes where the light source may be positioned.

664



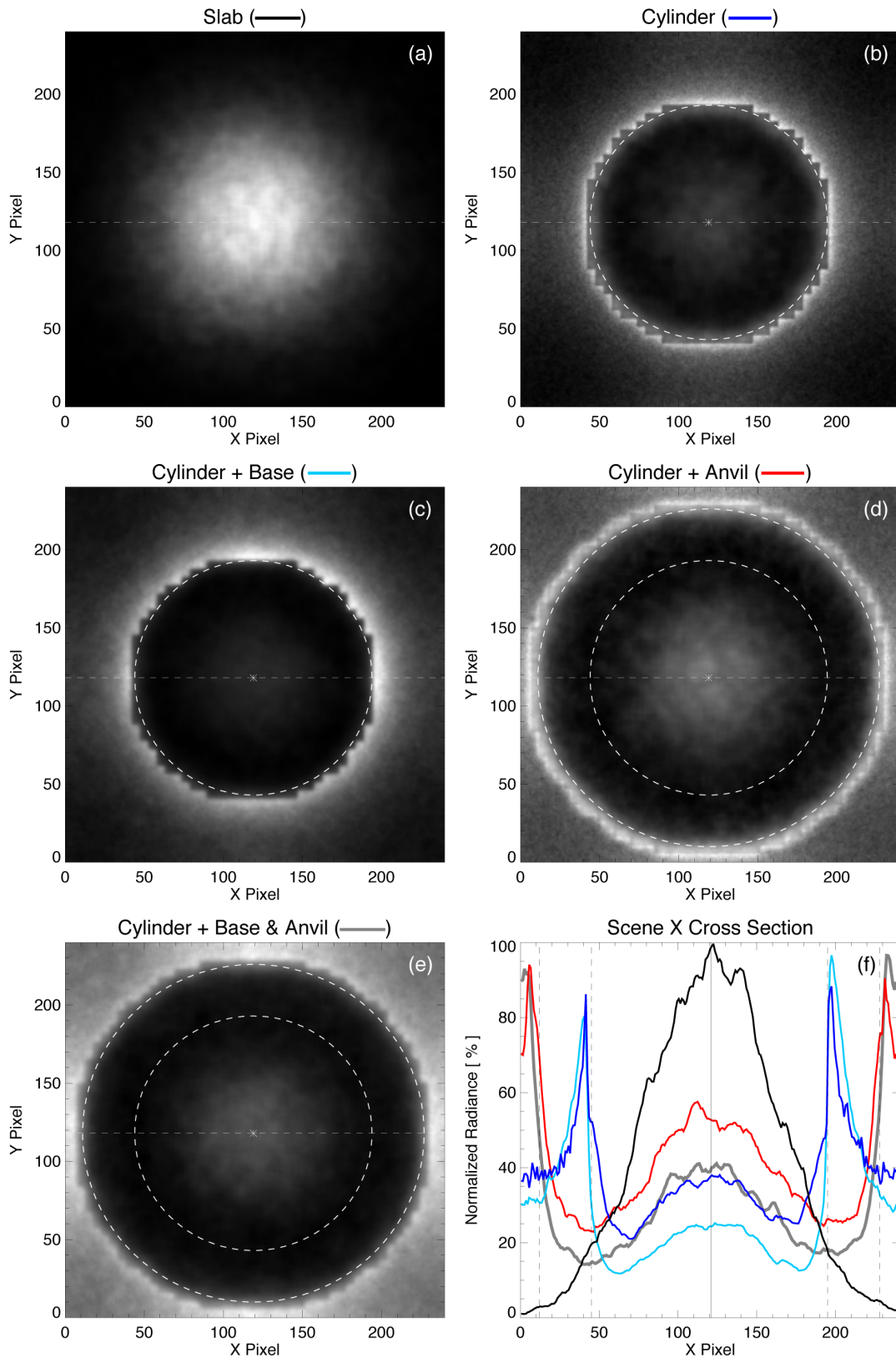
665  
 666  
 667  
 668  
 669  
 670

**Figure 3.** Source pixel (solid lines) and scene max (dashed lines) radiance from a surface-level  $10^9 \text{ W}$  source illuminating each cloud geometry (colors) with varying cloud extinction coefficients and optical depths.



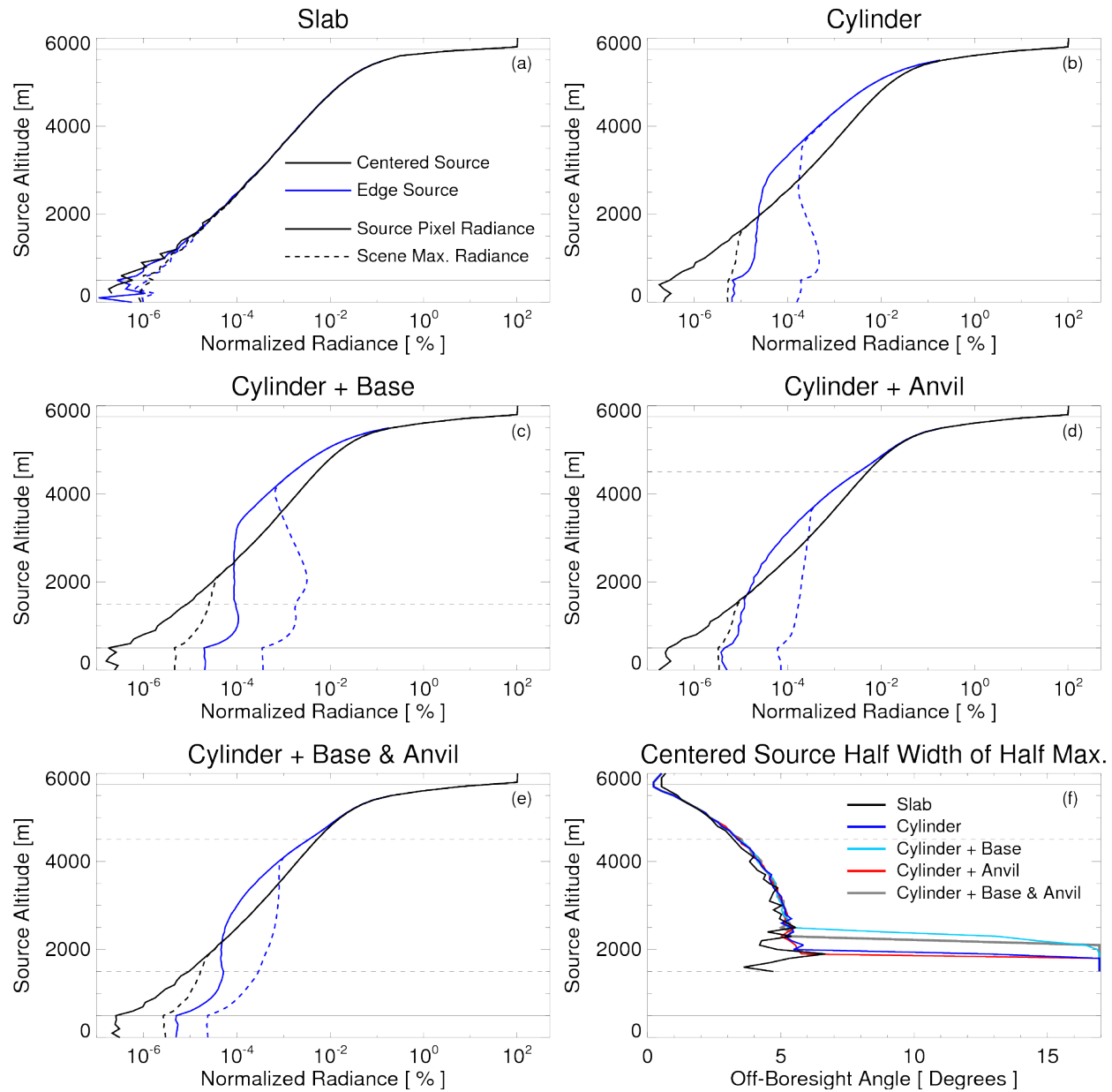
671  
672

673 **Figure 4.** Radiance patterns from a surface-level source illuminating a Slab (a), Cylinder (b),  
674 Cylinder + Base (c), Cylinder + Anvil (d), and Cylinder + Base & Anvil (e) cloud with an overall  
675 optical depth of 160. The cloud center is indicated with an asterisk symbol. Radiance cross  
676 sections along the imager X axis (dashed lines in a-e) are shown in (f) where the colors  
677 corresponding to each cloud are indicated in the titles for a-e. Radii corresponding to the bases of  
678 the primary cylinder (inner) and anvil cloud layer (outer) are shown as dashed circles in (a-e)  
679 (where present) and dashed vertical lines in (f).



680  
681  
682

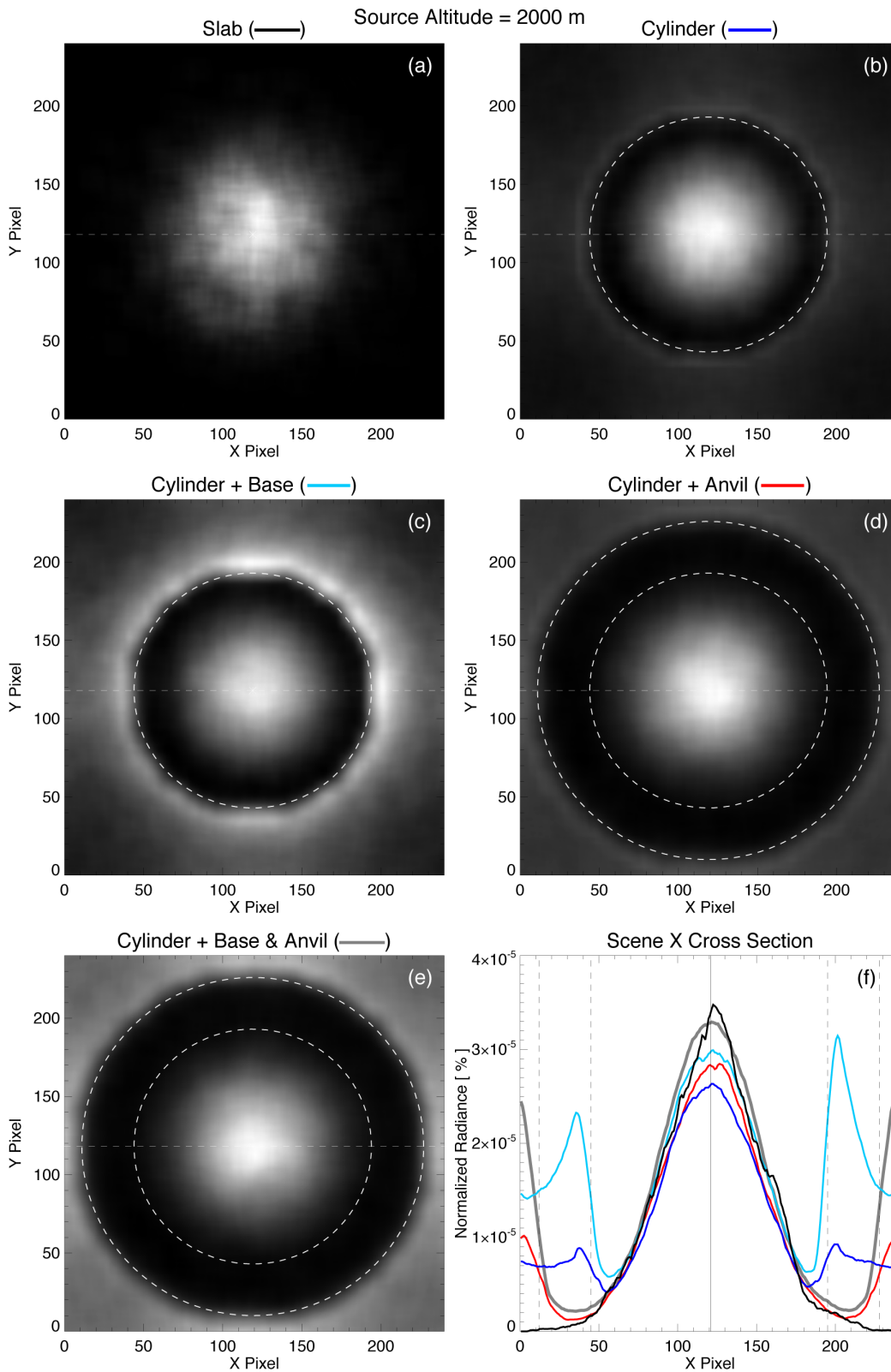
**Figure 5.** The same as Figure 4, but for the radiance patterns from a surface-level source illuminating clouds with an overall optical depth of 320.



683  
684  
685  
686  
687  
688  
689  
690  
691  
692  
693  
694

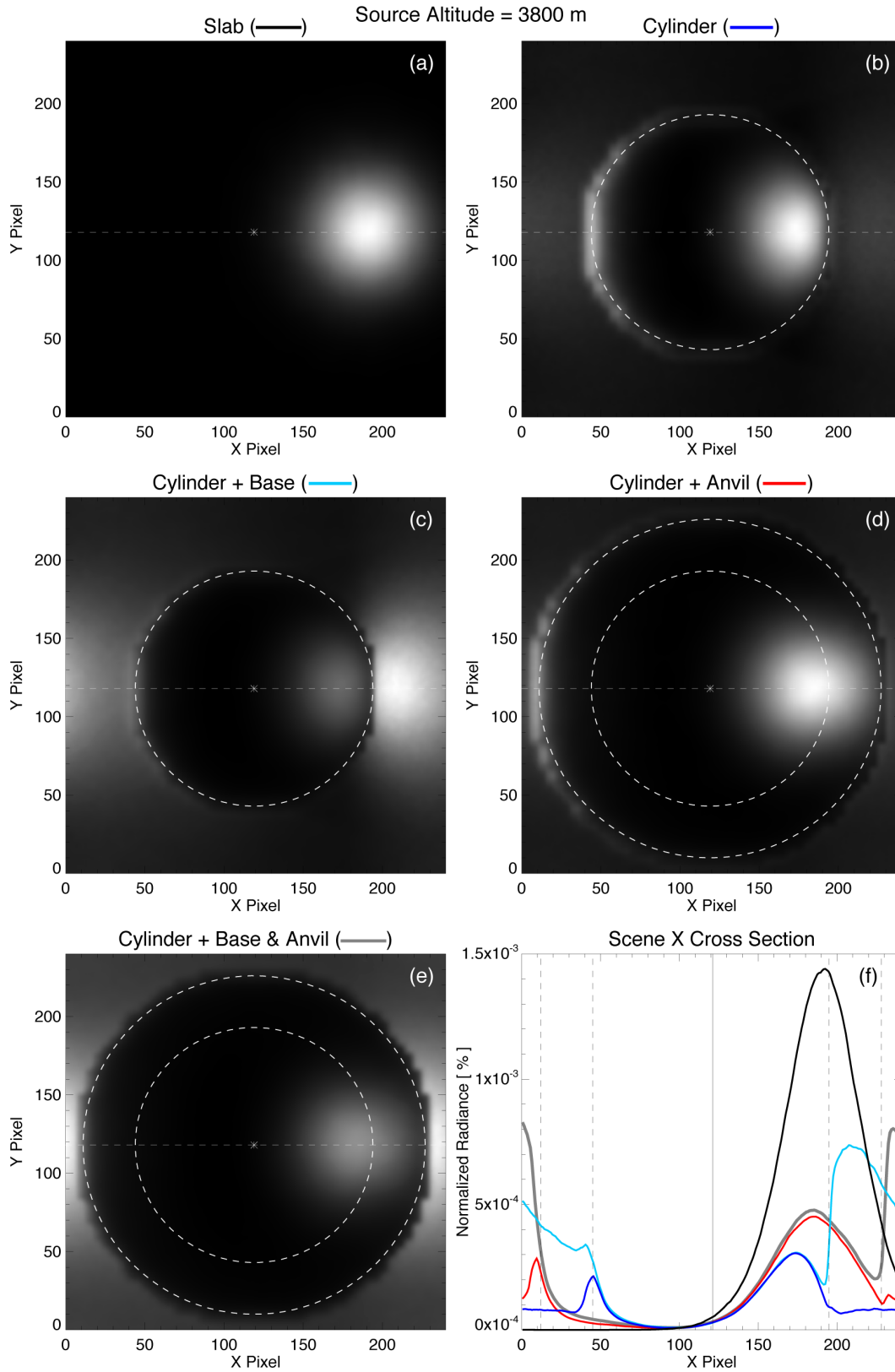
**Figure 6.** Profiles of the source pixel (solid lines) and scene max (dashed lines) radiance from centered (black) and edge (blue) sources at various altitudes illuminating Slab (a), Cylinder (b), Cylinder + Base (c), Cylinder + Anvil (d), and Cylinder + Base & Anvil (e) clouds with an overall optical depth of 400. Radiances are normalized relative to an unobstructed source at the cloud top (i.e., 100% at 5750 m). The Half Width of Half Maximum for each cloud type and source altitude above 1500 m is calculated in (f). The overall boundaries of each cloud layer are indicated with horizontal solid black lines, while the altitudes of the base layer and anvil cloud layer are indicated with dashed lines.

695



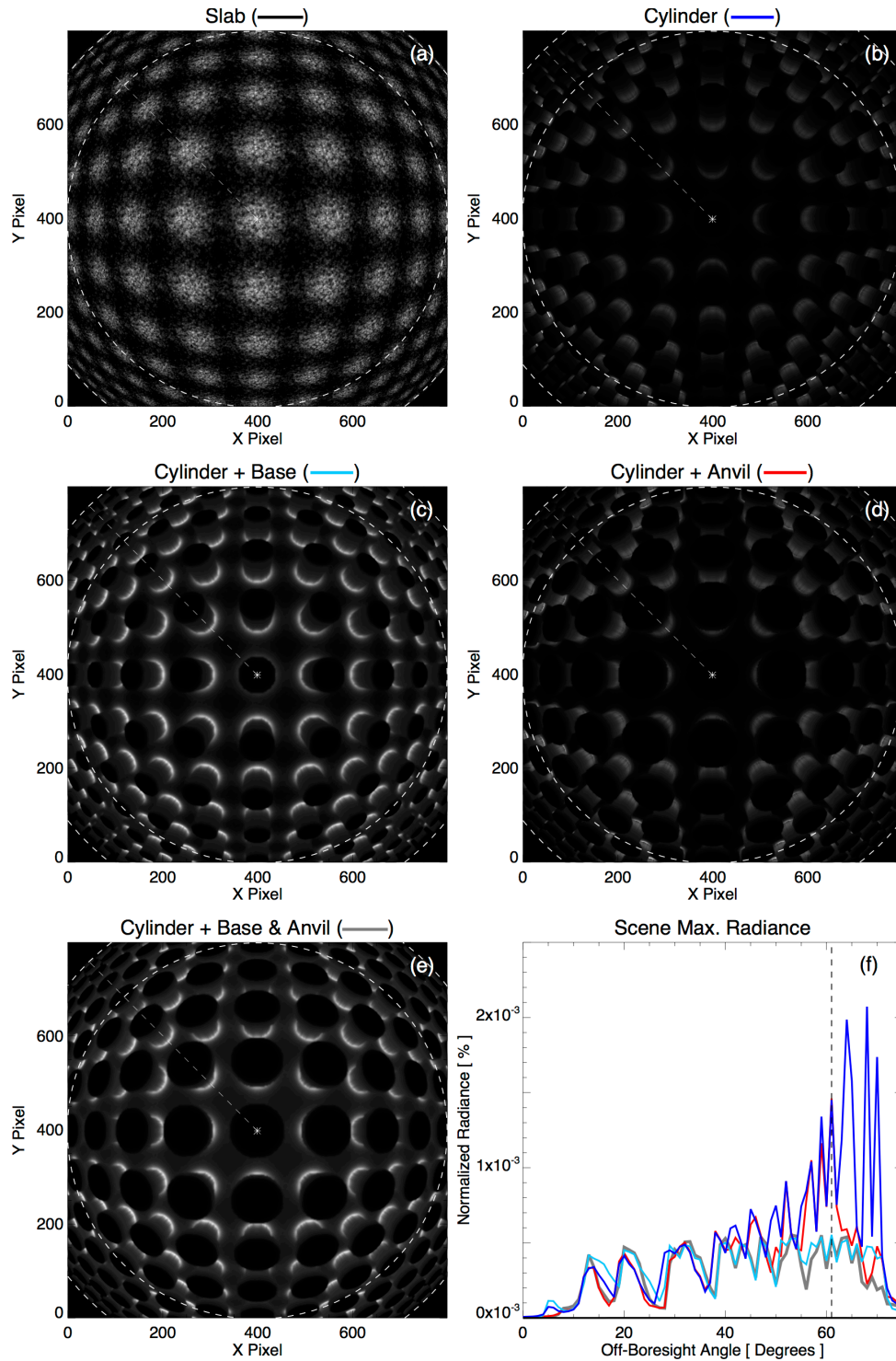
696  
697  
698

**Figure 7.** As in Figure 3, but for radiance patterns from a centered source located at 2000 m altitude illuminating clouds with an overall optical depth of 400.

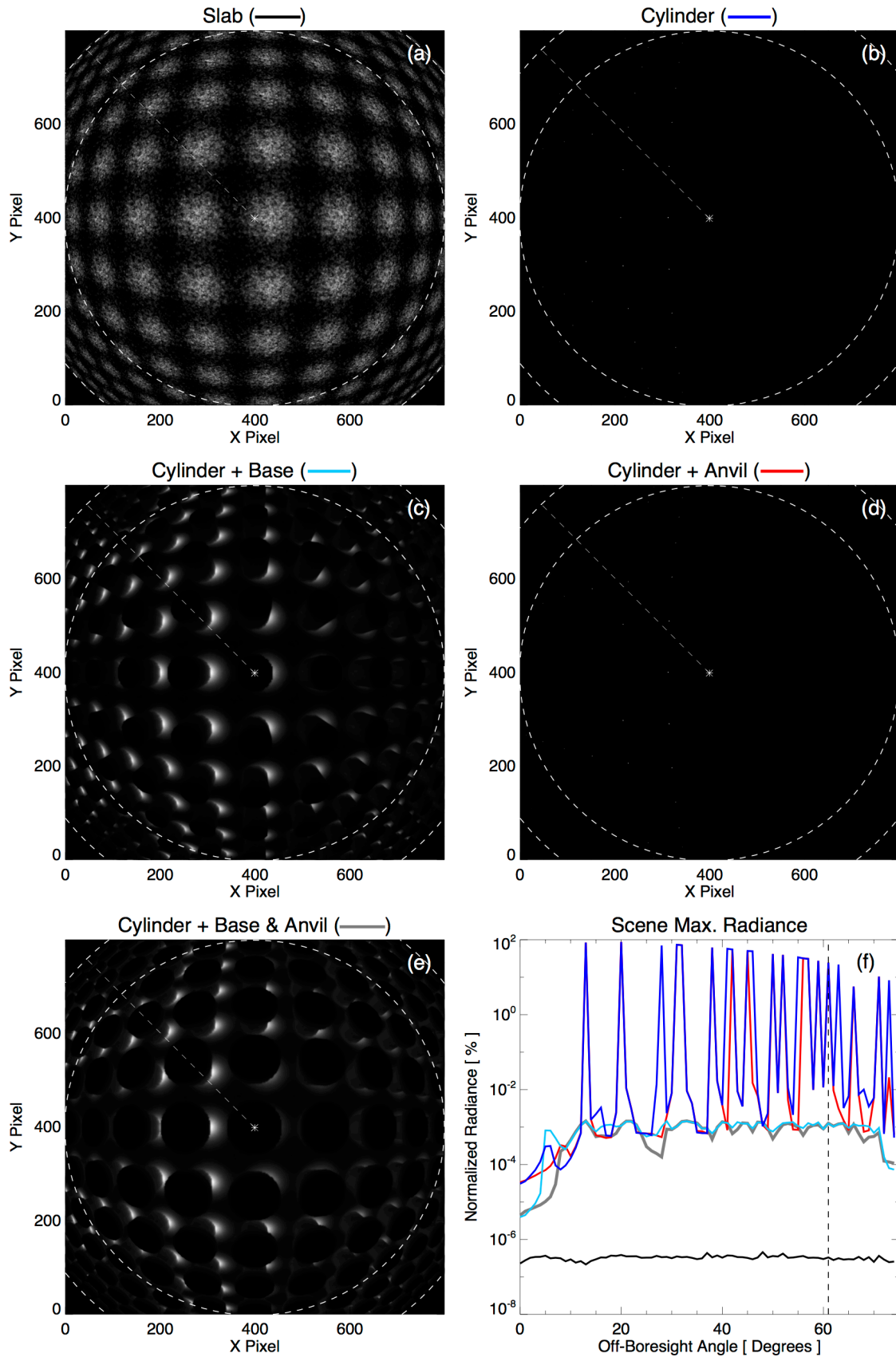


699  
700  
701

**Figure 8.** As in Figure 3, but for radiance patterns from an edge source located at 3800 m altitude illuminating clouds with an overall optical depth of 400.



702  
 703 **Figure 9.** Radiance patterns (a-e) from multiple cloud tiles illuminated by centered surface-level  
 704 sources (with a 100 m horizontal grid spacing) over an expanded 120° imager FOV. The radii  
 705 corresponding to the nominal imager FOV (inner) and horizon (outer) are indicated with dashed  
 706 circles. Radial cross sections of peak radiance (radial dashed line in a-e) for each cloud type are  
 707 shown in (f) as a function of off-boresight angle. The edge of the nominal imager FOV is  
 708 indicated with a dashed vertical line in (f). As in Figure 6, radiance is normalized relative to an  
 709 unobscured cloud-top source.



710  
711

**Figure 10.** As in Figure 9, but for surface-level sources near the edge of the primary cylinder.